CHEMISTRY & SUSTAINABILITY

CHEMSUSCHEM

ENERGY & MATERIALS

Accepted Article

Title: Tailoring the porosity in iron phosphosulfide nanosheets to improve performance of photocatalytic hydrogen evolution

Authors: Jian Zhang, Fang Feng, Yong Pu, Xing-Ao Li, Cher Hon Lau, and Wei Huang

To be cited as: *ChemSusChem* 10.1002/cssc.201900789

Link to VoR: http://dx.doi.org/10.1002/cssc.201900789

A Journal of

ChemPubSoc Europe

WILEY-VCH

www.chemsuschem.org

Tailoring the porosity in iron phosphosulfide nanosheets to improve performance of photocatalytic hydrogen evolution

Jian Zhang,[a],[b] Fang Feng,[b] Yong Pu, [a] Xing'ao Li,*[a],[b] Cher Hon Lau,[c] and Wei Huang*[b],[d]

Abstract: Metal sulfide photocatalysts are typically required during water splitting to produce hydrogen. However, the rapid recombination of photogenerated electron-hole pairs in these highly unstable photocatalysts has restricted hydrogen production to small scale batch reactions. In this work, we demonstrated the use of porous transitional metal thiophosphites to enable continuous long-term hydrogen production via photocatalysis. This bandgap (2.04 eV) was essential for generating hydrogen at a rate of 305.6 μmol h^{-1} g^{-1} – 180 % faster than non-porous $FePS_3$ nanosheets. More importantly, the high in-plane stiffness of these ~7 nm thick porous $FePS_3$ nanosheets ensured structural stability during 56 hours of continuous photocatalysis reactions. The reaction results with D_2O instead of H_2O indicate that hydrogen come from H_2O mainly. Besides, sacrificial reagent (triethylamine) is photodegradated into diethylamine and acetaldehyde via monoelectronic oxidation process from the results of HPLC and LC-MS. This synthesis strategy reported for $FePS_3$ PNSs pave a new pathway for designing other di-anion based inorganic nanocrystals in hydrogen energy applications.

Introduction

The conversion of solar energy into chemical energy can be achieved by splitting water into hydrogen using efficient photocatalysts derived from abundant earth-metals.[1-3] However, most photocatalysts suffer from the rapid recombination of photogenerated electron-hole pairs within 10 ns, drastically limiting hydrogen production in small scale batch reactions.[4,5] To overcome this drawback, strategies such as metallic or non-metallic element doping,[6-8] heterojunction construction,[9-11] and co-catalyst merging[12-14] have been developed to increase the separation and migration efficiency of charge carriers during photocatalytic hydrogen generation. Compared to traditional oxide photocatalysts such as TiO_2,[15] ZnO,[16] WO_3,[17] Fe_2O_3,[18] $BiVO_4$,[19] $BiFeO_3$,[20] $ZnGa_2O_4$,[21] sulfide semiconductors are more active for photocatalytic water splitting. This is due to their better photoresponse range. However, sulfide semiconductors are susceptible to photo-corrosion (S^{2-} + h → S) and hence are highly unstable.[22,23] This can be overcome by rapid depletion or migration of photogenerated holes on the valence band of catalysts.

A new class of layered metal phosphorus trichalcogenides with a general formula MPX_3 (M = Fe, Mn, Ni, Cd, Zn; X = S or Se) have attracted increasing attentions recently.[24,25] The metal atom of these layered structures is typically sandwiched between chalcogen atoms, forming an in-plane X-M-X configuration. This is beneficial for the hydrogen evolution reaction (HER) as the ratio of exposed chalcogen atoms i.e. active hydrogen production sites is enhanced.[24,26-28] A distinctive characteristic of MPX_3 structures is the wide-range band gap that can also be exploited for optoelectronic applications in a broad wavelength range.[29] Wang et. al. synthesized $NiPS_3$ photocatalyst nanosheets (a few atomic layer thick) and employed these materials to produce hydrogen under sunlight without using any sacrificial reagents.[30] Likewise $MnPS_3$, $MnPSe_3$ nanosheets,[31] and monolayer $FePS_3$ quantum sheets,[32] these ultrathin $NiPS_3$ nanosheets are highly unstable due to drastic losses in catalytic activity after long-term batch hydrogen generation. Clearly, the morphology and size of MPS_3 nanosheets can significantly impact on the behavior of photo-generated charge carriers.

Enlightened by this observation, here we synthesized $FePS_3$ porous nanosheets (PNSs) with uniform topography using our previously-reported one-step sulfurphosphidation method.[33] When compared to non-porous i.e. smooth $FePS_3$ nanosheets, the porosity of our novel structure was crucial for enhancing photocatalytic hydrogen production rates by 180 %, reaching 305.6 μmol h^{-1} g^{-1}. This was ascribed to the generation of hydrogen bubbles on rougher catalyst surfaces, which radically increased the efficiency.[34] Crucially, the enhanced photocatalytic activity of these novel structures was maintained even after continuous, long-term operation. Besides, mechanistic studies on the role of sacrificial reagents were performed. This unprecedented work potentially showcases a facile, universal synthesis protocol for 2D metal phosphosulfide nanosheets while setting a feasible criterion to evaluate the practicability of photocatalysts for hydrogen evolution.

2. Results and Discussion

2.1. Morphology of nanomaterials

SEM and TEM micrographs in Figure 1 clearly demonstrated the differences in shape, size and porosity between smooth and porous $FePS_3$ nanosheets. Macroscale or quantum sheets of MPX_3 structures are typically produced by complex techniques that require expensive and sophisticated equipment such as chemical vapor transport[35] and methods that are difficult to control i.e. liquid exfoliation.[32] Contrarily, our 7 nm-thick

[a] Dr. J. Zhang, Y. Pu, Prof. X. Li
New Energy Technology Engineering Lab of Jiangsu Province, School of Science, Nanjing University of Posts & Telecommunications (NUPT), Nanjing 210023, P. R. China.
E-mail: lxahbmy@njupt.edu.cn
[b] Dr. J. Zhang, Ms. F. Feng, Prof. X. Li, Prof. W. Huang
Key Laboratory for Organic Electronics and Information Displays & Institute of Advanced Materials (IAM), Jiangsu National Synergetic Innovation Center for Advanced Materials (SICAM), Nanjing University of Posts & Telecommunications, Nanjing 210023, P. R. China.
[c] Dr. C. Lau
University of Edinburgh, School of Engineering, Robert Stevenson Rd, Kings Building, Edinburgh EH9 3FB, Midlothian, Scotland.
[d] Prof. W. Huang
Shaanxi Institute of Flexible Electronics, Northwestern Polytechnical University, 127 West Youyi Road, Xi'an, 710072, Shaanxi, P. R. China.
E-mail: iamwhuang@njupt.edu.cn
Supporting information for this article is given via a link at the end of the document.

uniformly-shaped $FePS_3$ nanosheets (NSs) with length ~50 nm could be produced using a facile sulfur-phosphidation approach. The only morphological difference between the smooth and porous $FePS_3$ NSs was the presence of tiny dark spots in the porous nanomaterials. The morphologies including thickness and porosity of both the $FePS_3$ PNSs ans NSs were validated by TEM micrographs (Figure 1c,d). We observed uniformally structured distinctive lattice fringes of $FePS_3$ (PNSs) with a spacing of 0.32 nm resulting from the (002) plane of $FePS_3$.[36] STEM-HAADF and EDS mapping analyses indicated a homogeneous distribution of Fe, S, and P throughout the $FePS_3$ NSs and PNSs, verifying the alloy composition of the ternary system (Figure 1e and f). From Figure 1f, we also observed the presence of pores in $FePS_3$ (PNSs). Meanwhile, EDS mapping spectrum also revealed that the atomic ratio of Fe : P : S was close to 1 : 1 : 3, suggesting that the precise elemental composition ratio of this nanomaterial was identical to $FePS_3$. Besides, EDS (Figure S1) and ICP-AES (Figure S2) results also confirm the similar element content of $FePS_3$.

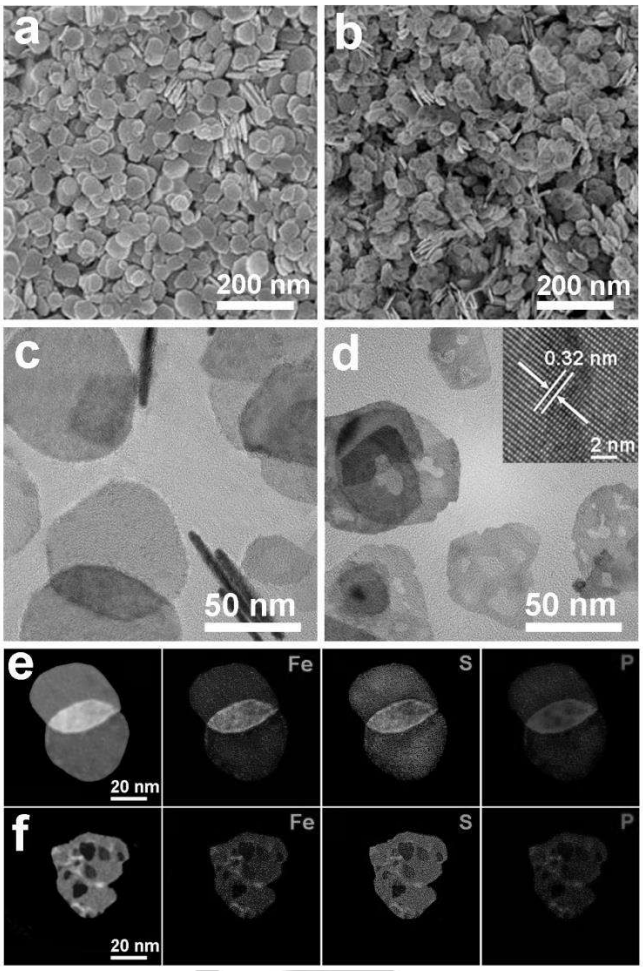

Figure 1. SEM micrographs of $FePS_3$ NSs (a) and PNSs (b). TEM images of $FePS_3$ NSs (c) and PNSs (d). Inset of d: HRTEM image of the $FePS_3$ PNSs. Scanning transmission electron microscopy in high angle annular dark field (STEM-HAADF) and energy dispersive spectroscopy (EDS) mapping (e and f) micrographs of $FePS_3$ NSs and PNSs, respectively.

The XRD spectra of both the $FePS_3$ NSs and PNSs contained all peaks corresponding to the standard card of $FePS_3$ (JCPDS Card No. 30-0663),[37] indicating the high crystalline and phase purity of our synthesized nanocatalysts. An intense diffraction peak located at 13.8° along with three weak peaks at 27.8°, 42.5° and 57.6° could be indexed to (001), (002), (003), and (004) planes of $FePS_3$, respectively. Porosity in $FePS_3$ nanosheets did not cause any peak shifts i.e. the crystallinity of $FePS_3$ was retained even after different sulfur-phosphidation process. Compared to the smooth samples, the diffraction peaks of porous $FePS_3$ nanosheets exhibited similar features but with lower intensities (Figure 2a, red curve). Raman scattering spectra obtained with an excitation wavelength of 532 nm revealed that vibrational bonding in both $FePS_3$ NSs and PNSs were identical. We observed two sets of Raman mode vibrations that could be attributed to the Fe and P_2S_6 components of the $FePS_3$ crystal system. As reported elsewhere,[38] peaks centered at 588, 375, 279, 245, and 216 cm^{-1} could be assigned to the E_g^3, A_{1g}^2, E_g^2, A_{1g}^1, and E_g^1 modes of $FePS_3$ (Figure 2b). The E_g modes (E_g^1, E_g^2, and E_g^3) represented in-plane vibrations of the P_2S_6 unit (tangential vibration of the P-P bond). Meanwhile, intra-layer modes underpinned a slight Raman shift in thinner structures, causing the observed shifts in both peak positions (Figure 2b).[38] The sharp features in Raman spectra also suggested that both the $FePS_3$ NSs and PNSs could retain a stable structure.[25]

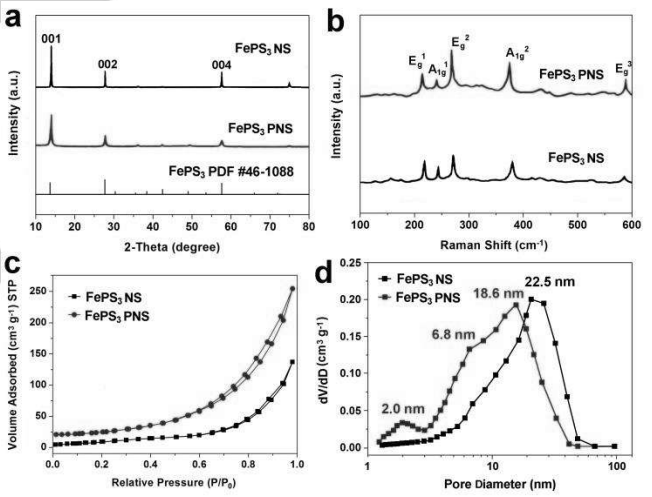

Figure 2. (a) XRD patterns, and (b) Raman spectra of as-synthesized $FePS_3$ NSs (black) and PNSs (red). (c) The N_2 adsorption-desorption isotherm, and pore-size distribution curves of (d) as-synthesized $FePS_3$ NSs and PNSs.

The specific surface areas of $FePS_3$ nanosheets studied here were determined from N_2 adsorption desorption isotherms (Figure 2c). We observed a type IV isotherm at high relative pressure (P/P_0) and a H1 hysteresis loop in the relative pressure range of 0.66-0.98 P/P_0, implying the presence of mesopores. The Brunauer-Emmett-Teller (BET) specific surface area of the $FePS_3$ PNSs was about 91.2 $m^2\ g^{-1}$ – nearly twice as large as that of smooth $FePS_3$ nanosheets (46.6 $m^2\ g^{-1}$). The porosity

within each finely dispersed nanosheet was key to doubling the BET surface area. From the Barrett-Joyner-Halenda (BJH) method, we observed a broad (1 – 40 nm), trimodal pore size distribution in $FePS_3$ porous nanosheets. Main of these peaks were centered at 2.0, 6.8 and 18.6 nm, which was in good agreement with TEM characterization (Figure 2d). The dominant large pores were formed by the merger of numerous interconnected small pores during thermal treatment, while micropores that were beneficial for increasing the amount of photocatalytic active sites were formed from the release of CO_2 and H_2O during decomposition of the $Fe_2(CO_3)(OH)_2$ precursor in the preheating phase (400 °C for 2 h).[39] As expected, for smooth $FePS_3$ NSs, no obvious peak was detected below 10 nm.

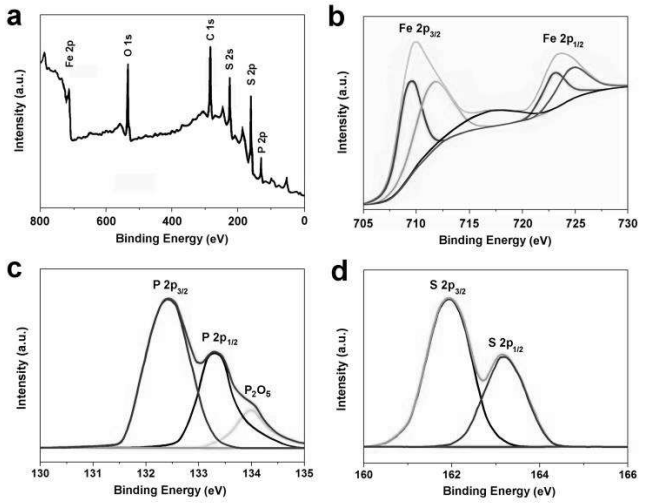

Figure 3. XPS spectra of the $FePS_3$ PNSs: full XPS spectra (a); High-resolution XPS spectra of Fe 2p (b), P 2p (c), and S 2p (d).

XPS characterization was employed here to analyze the atomic species and bonding nature present in $FePS_3$ PNSs photocatalysts i.e. the ratio of exposed chalcogen atoms. From the wide XPS spectrum, we observed P 2p, S 2p, C 1s, S 2s, O 1s, and Fe 2p peaks with binding energies of 132.4, 162.4, 226.0, 284.8, 531.7, and 710.7 eV respectively (Figure 3a). C 1s and O 1s peaks could attribute to the conductive substrates in the testing process. For the Fe 2p spectra (Figure 3b), we observed two peaks with binding energies of 709.9 and 723.2 eV which corresponded to the $2p_{3/2}$ and $2p_{1/2}$ levels of Fe^{2+}, respectively.[40] Meanwhile, peaks with binding energies of 133.3 and 132.4 eV could be ascribed to spin-orbit splitting in P $2p_{1/2}$ and P $2p_{3/2}$, respectively (Figure 2c). Compared to the binding energies of pure P (129.1 eV)[41] and Fe_2P (130.0 eV)[42], the 2.5 eV increment in P binding energy of $FePS_3$ (Figure 3c) could be attributed to electron donation from P to the S-containing ligand in $FePS_3$ PNSs. The weak peak with a binding energy of 134.0 eV was indicative of the oxidation state of P $2p_{3/2}$ (P_2O_5).[43] Similar to the P 2p core level spectra, we also observed two intense peaks with binding energies of 161.9 and 163.3 eV. These peaks were due to the spin-orbit split $2p_{3/2}$ (Ni-S) and $2p_{1/2}$ (P-S) binding energies, respectively.

The absorption properties of $FePS_3$ samples were measured with UV/vis diffuse reflectance absorption and ultraviolet photoelectron spectroscopy (UPS). At both visible and UV light ranges, a broad absorption peak was present in $FePS_3$ NSs (Figure 4a, black curve). Porosity in $FePS_3$ nanosheets intensified light absorption, especially in the UV range. This absorption enhancement also underpinned better solar energy conversion efficiences in other mesoporous or porous photocatalysts by maximizing light adsorption.[44] According to the Kubelka-Munk theory,[45] the bandgap energy of two catalysts can be estimated by transforming the UV/vis diffuse reflection absorption spectra into a Tauc plot where the X and Y axes correspond to and $h\mu$ $(\alpha h\mu)^{1/2}$, respectively.[46] From the intercept of the tangent to $h\mu$ (Figure 4b), the bandgap values of smooth and porous $FePS_3$ nanosheets were estimated to be 1.97 and 2.04 eV, respectively in neutral environment.[47,48] After subtracting the excitation energy (21.22 eV) (the width of He I UPS spectra), the valence band value was calculated to be -5.57 eV (*vs* E_{Vacuum}) for $FePS_3$ porous nanosheets (-21.22 – (-16.67) – 1.05). Accordingly, the valence band value of porous $FePS_3$ nanosheets was -5.57 eV, while its conduction band value (E_c) was -3.53 eV (Figure 4d). The band gap was large enough to cover both oxidation ($H_2O \rightarrow O_2$) and reduction ($H^+ \rightarrow H_2$) potentials of H_2O whilst generating potential differences for hydrogen and oxygen generation of 0.47 eV and 0.34 eV, respectively. This combination could potentially facilitate photocatalytic water splitting using porous $FePS_3$ nanosheets.

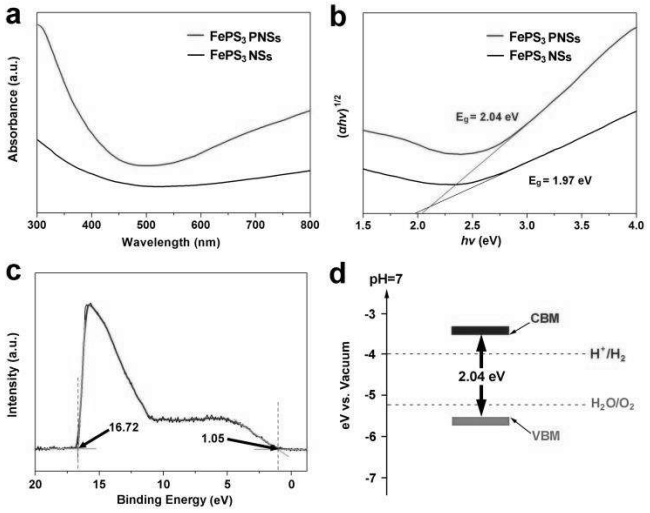

Figure 4. UV/vis diffusive reflectance absorption spectra (a) and the estimated bandgap potential (b) of $FePS_3$ NSs and PNSs. Ultraviolet photoelectron spectra (UPS) (c) and schematic depicting the specific energy levels (d) of $FePS_3$ PNSs.

2.2. Hydrogen generation

Firstly, the effects of sacrificial reagents, including triethylamine (TEA), triethanolamine (TEOA), ethanol (EtOH) and methanol

(MeOH), on the hydrogen production from water over $FePS_3$ NSs and PNSs were studied under 300 W Xe lamp irradiation (Figure S3). Obviously, the highest hydrogen production rate of the photocatalysts was achieved in 10% TEA solution. Specifically, the hydrogen evolution rate from smooth $FePS_3$ nanosheets reached up to 166.2 μmol h^{-1} g^{-1} (Figure 5a, TEA as sacrificial reagents), while the porous nanosheets exhibited a significantly higher rate of 305.6 μmol h^{-1} g^{-1}. The quantum efficiency of porous $FePS_3$ nanosheets was dependent on the irradiation light wavelength (Figure 5b). The highest QE value of 8.3% was detected at 400 nm. The rapid decay of photocatalytic activity of metal sulfides (S^{2-} + h → S) was the main cause of instability in these nanomaterials.[49] Here we show that this could be overcome using di-anions (P and S) with different electronegativities that enhanced electron delocalization of the metal atoms to suppress photo-corrosion.[50] The photostability of our smooth and porous $FePS_3$ nanosheets were maintained even after 7 cycles of batch tests over 56 h, outperforming current state-of-the-art sulphide-based photocatalysts. The hydrogen production efficiency of $FePS_3$ NSs and PNSs revealed negligible decay, demonstrating unprecedented photostability (Figure 5c).

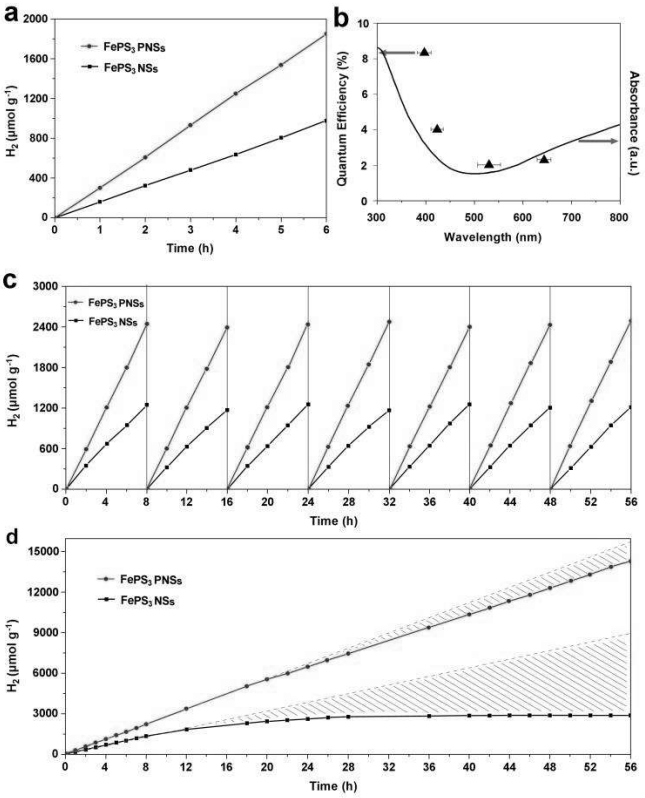

Figure 5. Photocatalytic hydrogen evolution rates of the $FePS_3$ NSs and PNSs (a) (200 mL deionized water with 10% triethylamine (TEA) as sacrificial reagents, 300 W Xe lamp) and monochromatic light quantum efficiency of porous $FePS_3$ nanosheets (b). Uncontinuous (c) and continuous (d) cycling measurements of hydrogen generation of the smooth and porous $FePS_3$ nanosheets (Blue dotted lines = ideal hydrogen production rates).

Hydrogen generation cycle measurements are a benchmark to evaluate photostability.[51-53] Upon illumination, hydrogen bubbles will be generated and might accumulate on catalyst surfaces during photocatalysis. Complete desorption of hydrogen molecules could be achieved by reducing the system pressure to a vacuum state after every cycling, akin to a pressure swing adsorption setup. This would benefit hydrogen production as the removal of hydrogen from the catalyst surface which could drive the reaction equilibrium towards producing more hydrogen. For contrast, continuous tests[54,55] were also performed using $FePS_3$ NSs and PNSs. In reality, hydrogen was produced at a steady rate that was ~10 % lower than an ideal situation (Ideal: 15.583 mmol *vs*. Reality: 13.787 mmol) over 56 h. Meanwhile, for smooth $FePS_3$ nanosheets, the hydrogen production rate was drastically reduced after 12 h, and then reached almost zero during the last 28 h of testing. hydrogen production was only observed over a period of 28 h when smooth $FePS_3$ nanosheets were employed (Figure 5d); demonstrating a half photocatalytic lifetime when compared to $FePS_3$ PNSs. This difference in photocatalytic lifetimes could be attributed to the surface roughness. Porous nanosheets tend to burst larger hydrogen bubbles into smaller bubbles, and wick them away from the surface – similar to bubbles at the microstructured surface of a lotus leaf.[34] Larger hydrogen bubbles could be generated easily on the smooth surfaces of $FePS_3$ NSs that might consequently cover the catalytic active site and suppress the photocatalytic activity and reduce lifetime.[56] TEM micrographs and XRD analyses (Figures S4 and S5, Supporting Information) of $FePS_3$ PNSs also demonstrated that the morphology and crystallinity of porous photocatalysts remained intact after 56 h of continuous testing, validating the superb photo-stability of these porous nanostructures. To further evaluate the photocatalytic activity and stability, the same photocatalytic system was employed in pure water without any sacrificial reagents. Unexpectedly, the hydrogen production rates of both smooth and porous $FePS_3$ nanosheets were 72.9 and 118.3 μmol g^{-1} h^{-1}, respectively (Figure S6). The cyclic tests over 31 h also showed good photo-stability (Figure S7). Compared to the results of the effects of sacrificial reagents (Figure S3), we can find MeOH and EtOH were useless for increasing the rate of hydrogen generation in our photocatalytic system.

Figure 6a shows the photocurrent density *vs*. potential (Ag/AgCl) curves for $FePS_3$ NSs and PNSs under dark and light illumination. The dark current from -0.9 V to 0.3 V corresponding to both the samples exhibit negligible. Upon illumination, the photocurrent densities (the onset potential is around -0.9 V) of both $FePS_3$ photoelectrodes show improvement with increasing applied potential. The $FePS_3$ PNSs photoelectrode showed a maximum photocurrent value of 0.95 mA cm^{-2} at 0.3 V *vs.* Ag/AgCl, which is 2.3 times that of smooth sample. Transient light responses of $FePS_3$ NSs and PNSs photoelectrodes also performed at 0 vs. Ag/AgCl with light on (for 50 s) and off (for 50 s) over 6 cycles (Figure S8). For porous nanosheets, a negligible photocurrent spike value due to the slight transient effect in power excitation was observed immediately[57] and returned to a steady value of ~0.6 mA cm^{-2} quickly,

demonstrating a stable photoelectrochemical process. Electrochemical impedance spectroscopy revealed the interface charge transfer character of $FePS_3$ NSs and PNSs. The arc diameters in the EIS plot (Figure 6b) of porous $FePS_3$ nanosheets were smaller than their smooth counterparts, indicating a lower resistance of the interfacial charge transfer between conductive substrates and $FePS_3$ porous nanocatalysts.

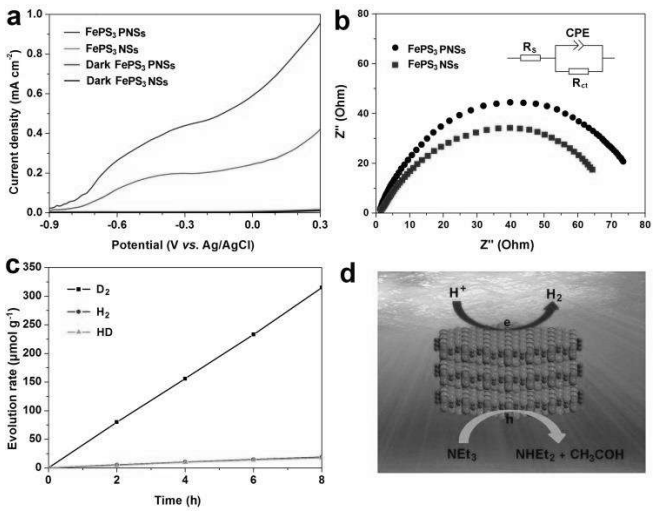

Figure 6. Photocurrent density-potential (J-V) curves vs. Ag/AgCl (a) and electrochemical impedance spectroscopy (EIS) plots in dark (b) of $FePS_3$ NSs and PNSs. (c) The rate of evolution of gaseous products in the photocatalytic reaction of 10% TEA with D_2O. (d) Schematic of photocatalytic reaction processes for the $FePS_3$.

2.3. Degradation Mechanism of Sacrificial Reagents

As Bahnemann[58] and Jin[59] claimed, for photocatalysis hydrogen generation system with sacrificial electron donors, hydrogen will be formed through both the direct reductive (H_2O) as well as the indirect oxidative (sacrificial reagent) paths. Therefore, the role of optimal sacrificial reagent (TEA) was investigated to understand the mechanism of photocatalytic hydrogen production over the $FePS_3$ PNSs. Diethylamine (DEA) and acetaldehyde are main products during the photocatalysis process (20 h) from the results of HPLC (Figure S9) and LC-MS (Figure S10) (74.0 and 102.1 mass are indexed to DEA and TEA, respectively). Besides, D_2O was used instead of H_2O for the photocatalytic hydrogen evolution with the $FePS_3$ PNSs nanocatalyst (10% TEA) to represent the yield of photocatalytic hydrogen generation accurately as shown in Figure 6c. The rates of gaseous products including D_2, H_2, and HD are 39.2, 3.8, and 3.7 μmol h^{-1} g^{-1}, respectively. Intuitively, the reaction results with D_2O instead of H_2O indicate that H_2O may be a main hydrogen source, similar with the previous literatures such as g-C_3N_4[60] and CdS[61] catalysts. Compared with the rate of hydrogen evolution from H_2O (305.6 μmol h^{-1} g^{-1}), the low rate of gaseous products may attribute to the difference between D^+ and H^+. According to the recent reports, sacrificial organic electron donors may be a main hydrogen source on the TiO_2 based catalyst system.[62,63] On the basis of the above results, a possible mechanistic explanation of the improved photocatalytic hydrogen generation on the FePSs system with TEA as a sacrificial reagent has been proposed as shown in Figure 6d.

3. Conclusions

In summary, iron phosphosulfide porous nanosheets ($FePS_3$) photocatalysts with remarkable photocatalytic activity and photostability were synthesized *via* a facile in-situ thermal sulfurphosphidation process. Under Xe lamp driven conditions, porous $FePS_3$ nanosheets exhibited enhanced photocatalytic hydrogen production rates (305.6 μmol h^{-1} g^{-1}) when compared to smooth $FePS_3$ nanosheets (166.2 μmol h^{-1} g^{-1}). More importantly, the unprecedented photo-stability of porous $FePS_3$ nanosheets was demonstrated through a 56 h continuous hydrogen production test. The proposed strategy for fabricating porous di-anion semiconductor photocatalysts with high specific surface areas might bring new opportunities in developing highly effective and durable photocatalysts for a wide range of sustainable energy conversion and production applications.

4. Experimental Section

4.1 Synthesis of $Fe_2(CO_3)(OH)_2$ precursor

Uniform $Fe_2(CO_3)(OH)_2$ nanosheets were synthesized by a simple hydrothermal process. All chemicals in this work are of analytical purity and used without further purification. 1.35 g of iron nitrate hexahydrate ($Fe(NO_3)_3{\cdot}9H_2O$, 98%, Sigma-Aldrich) was dissolved in 38 mL of distilled water to form a clear solution by magnetic stirring, After that, 0.11 g of urea ($CO(NH_2)_2$, AR, Shanghai Chemical Factory of China) and 0.04 g poly(vinylpyrrolidone) (PVP, AR, Shanghai Chemical Factory of China) were added successively. After 30 min of magnetic stirring , the mixture was transferred to a 50 mL Teflon-lined stainless autoclave and heated at 140 °C for 12 h. Upon cooling to room temperature naturally, the precipitate was collected by centrifugation and washed with distilled water and ethanol and dried in a vacuum oven at 50 °C for 12 h. The powder was collected and dried in a vacuum oven at 60 °C for 8 h.

4.2 Synthesis of $FePS_3$

Smooth $FePS_3$ nanosheets were synthesized by a one-step sulfur-phosphidation method with little modification.[33] The obtained $Fe_2(CO_3)(OH)_2$ precursor were placed at the downstream end of a tube furnace (outside the heating area of the furnace) and a 1:1 mixture of sulphur (Sigma-Aldrich, 99.5 %) and phosphorus (Sigma-Aldrich, 99.0%) powders was placed in alumina boat at the upstream side of the tube furnace. The furnace was first heated to 200 °C within 20 min and maintained for 15 min under Ar carrier gas (99.999%) at 50 sccm. After cooling to room temperature naturally, the alumina boat containing a thiophosphate (P_xS_y) paste-like product was moved to the upstream edge of the furnace, and the precursor vessel ($Fe_2(CO_3)(OH)_2$) was moved to the heating zone of the furnace. The furnace was then heated to 500 °C for 1 h to convert these precursors into $FePS_3$ before the furnace was cooled down naturally. To produce $FePS_3$ porous nanosheets, the precursor vessel was moved into the heating zone of the furnace which was heated to 400 °C for 2 h and then 500 °C for 1 h to complete the

transformation. Precursor $Fe_2(CO_3)(OH)_2$ can be decomposed to produce porous under 400 °C before sulfurphosphidation process.

4.3 Materials Characterizations

The morphologies of the samples were characterized by transmission electron microscopy (TEM) (FEI Tecnai F20) with an acceleration voltage of 200 kV. Scanning transmission electron microscopy (STEM) was performed using a FEI Titan 80-200 (ChemiSTEM) electron microscope operated at 200 kV, equipped with a high angle annular dark field (HAADF) detector, while compositional maps were obtained with energy dispersive spectroscopy (EDS) using four large solid-angle symmetrical Si drift detectors. Scanning electron microscopy (SEM) was performed on a Hitachi S-4800 scanning electron microscope. X-ray photoelectron spectra (XPS) were acquired on an ESCALAB MK II with Mg Kα as the excitation source. The valence band energy of the samples was analyzed on Thermo Scientific ESCALab 250Xi using Ultraviolet photoelectron spectra (UPS). The BET surface area was measured using the nitrogen gas adsorption-desorption method (TriStar II 3020) at 77 K. XRD measurements were carried out on a BRUKER D8 Advance X-diffractometer with Cu Kα radiation**.** Raman spectroscopy was performed with a laser micro-Raman spectrometer (Renishaw in Via, 532 nm excitation wavelength). UV/vis DRS were recorded on a Lambda 750 spectrophotometer equipped with an integrating sphere. Inductively coupled plasma atomic emission spectrometry (ICP-AES) analysis was performed on a Thermo ICAP-6300 instrument (USA). An Agilent 1260 high-performance liquid chromatograph (HPLC) equipped with a Phenomenex C18, 4 μm particle size analytical column coupled with a diode array detector was used. The mobile phases for TEA solutions were prepared by mixing water and methanol in a volume ratio of 75:25. In addition, an Agilent 6130 series quadrupole liquid chromatography mass spectrometry (LC-MS) system equipped with an electrospray ionization source and an atmospheric pressure chemical ionization source in the positive ion mode were used. Detection using Phenomenex C18, 3 μm particle size column (40 °C), and water/acetonitrile (95:5, v/v) as the mobile phase was carried out. The apparent quantum efficiency (QE) was measured under the same photocatalytic reaction condition. A power meter (1916-R Newport) was used for the measurement of light intensity. The QE plotted were estimated though several cut-off filters, and were calculated on the basis of the number of the incident photons in each wavelength region. Accordingly, each value is plotted in the middle of two cut-off wavelengths. The QE was calculated according to eq (1):

$$\mathrm{QE}[\%] = \frac{\text{number of reacted electrons}}{\text{number of incident photons}} \times 100 = \frac{\text{number of evolved } H_2 \text{ molecules} \times 2}{\text{number of incident photons}} \times 100 \quad (1)$$

4.4 Measurement of Photocatalytic Hydrogen Evolution

The photocatalytic hydrogen production experiments were carried out in a closed gas-circulation system. A 300 W Xe lamp served as the light source. In a typical photocatalytic experiment, 0.01 g of catalyst was dispersed in an aqueous solution (200 mL) containing 10% sacrificial reagents (triethylamine, triethanolamine, ethanol and methanol). Before irradiation, the system was vacuumed for about 30 min to remove the air inside and to ensure that the system was under the anaerobic condition. During irradiation, continuous stirring was applied to keep the samples in suspension. Evolved hydrogen was analyzed using a gas chromatograph (Shimadzu GC-14C). The J-V performance of the photoanodes was evaluated in a typical three-electrode arrangement, consisting of a $FePS_3$ photoanodes as the working electrode, Pt as the counter electrode, and Ag/AgCl (saturated KCl) as the reference electrode. The prepared samples were immersed in the electrolyte composed of 0.01 M Na_2SO_4 aqueous solution, which acts as the sacrificial hole scavenger. The electrolyte solution was continuously purged with N_2 to remove any dissolved oxygen before test.

Conflicts of interest

The authors declare no competing financial interest.

Acknowledgements

We acknowledge the National Natural Science Foundation of China (51602161, U1732126, 51872145, 61874060), the Key Project of National High Technology Research of China (2011AA050526), the Ministry of Education of China (No. IRT1148), the National Synergetic Innovation Center for Advanced Materials (SICAM), the Natural Science Foundation of Jiangsu Province, China (BM2012010), the Project Funded by the Priority Academic Program Development of Jiangsu Higher Education Institutions (PAPD, YX03001).

Keywords: $FePS_3$ • porous nanosheets • photocatalysis • hydrogen evolution • stability

References

[1] Y. Tachibana, L. Vayssieres, J. R. Durrant, *Nat. Photonics* **2012**, *6*, 511-518.
[2] J. Zhang, L. Wang, X. Liu, X. Li, W. Huang, *J. Mater. Chem. A* **201**5, *3*, 535-541.
[3] J. Mahmood, F. Li, S. Jung, M. Okyay, I. Ahmad, S. Kim, N. Park, H. Jeong, J. Baek, *Nat. Nanotechnol.* **2017**, *12*, 441-446.
[4] J. Tang, J. R. Durrant, D. R. Klug, *J. Am. Chem. Soc.* **2008**, *130*, 13885-13891.
[5] J. Cai, Y. Zhu, D. Liu, M. Meng, Z. Hu, Z. Jiang, *ACS Catal.* **2015**, *5*, 1708-1716.
[6] G. Zhang, M. Zhang, X. Ye, X. Qiu, S. Lin, X. Wang, *Adv. Mater.* **2014**, *26*, 805-809.
[7] B. Ma, D. Li, X. Wang, K. Lin, *Chemsuschem*, **2018**, *11*, 3871-3881.
[8] W. Chen, Z. He, G. Huang, C. Wu, W. Wu and X. Liu, *Chem. Eng. J.*, **2019**, *359*, 244-253.
[9] X. Cai, L. Mao, S. Yang, K. Han and J. Zhang, *ACS Energy Lett.*, **2018**, *3*, 932-939.
[10] J. Ran, W. Guo, H. Wang, B. Zhu, J. Yu, S. Qiao, *Adv. Mater.* **2018**, *30*, 1800128.
[11] W. Chen, T. Liu, T. Huang, X. Liu, X. Yang, *Nanoscale* **2016**, *8*, 3711-3719.
[12] Q. Li, B. Guo, J. Ran, B. Zhang, H. Yan, J. Gong, *J. Am. Chem. Soc.* **2011**, *133*, 10878-10884.
[13] J. Zhang, L. Qi, J. Ran, J. Yu, S. Qiao, *Adv. Energy Mater.* **2014**, *4*, 1301925.
[14] X. Zong, G. Wu, G. Ma, F. Wen, L. Wang, C. Li, *J. Am. Chem. Soc.* **2008**, *130*, 7176-7177.
[15] Q. Wang, J. Huang, H. Sun, Y. Ng, K. Zhang, Y. Lai, *Chemsuschem* **2018**, *11*, 1708-1721.
[16] X. Li, S. Liu, K. Fan, Z. Liu, B. Song, J. Yu, *Adv. Energy Mater.* **2018**, *8*, 1800101.
[17] J. Meng, Q. Lin, T. Chen, X. Wei, J. Li, Z. Zhang, *Nanoscale* **2018**, *10*, 2908-2915.
[18] J. Li, Q. Pei, R. Wang, Y. Zhou, Z. Zhang, Q. Cao, D. Wang, W. Mi, Y. Du, *ACS Nano* **2018**, *12*, 3351-3359.

[19] F. Tang, W. Cheng, H. Su, X. Zhao, Q. Liu, *ACS Appl. Mater. Interfaces.* **2018**, *10*, 6226-6234.
[20] P. Liu, H. Sun, X. Liu, H. Sui, Y. Zhang, D. Zhou, Q. Guo, Y. Ruan, *J. Am. Ceram. Soc.* **2017**, *100*, 3540-3549.
[21] P. Zhao, Y. Li, L. Li, S. Bu, W. Fan, *J. Phys. Chem. C* **2018**, *122*, 10737-10748.
[22] Z. Wang, J. Peng, X. Feng, Z. Ding, Z. Li, *Catal. Sci. Technol.* **2017**, *7*, 2524-2530.
[23] J. Zhang, Q. Zhang, L. Wang, X. Li, W. *Sci. Rep.* **2016**, *6*, 27241.
[24] R. Musmao, Z. Sofer, D. Sedmidubsky, S. Huber and M. Pumera, *ACS Catal.* **2017**, *7*, 8159-8170.
[25] K. Du, X. Wang, Y. Liu, P. Hu, M. I. B. Utama, C. K. Gan, Q. Xiong and C. Kloc, *ACS Nano*, **2016**, *10*, 1738-1743.
[26] Z. Wu, X. Li, W. Liu, Y. Zhong, Q. Gan, X. Li, H. Wang, *ACS Catal.* **2017**, *7*, 4026-4032.
[27] V. Nicolosi, M. Chhowalla, M. G. Kanatzidis, M. S. Strano, J. N. Coleman, *Science* **2013**, *340*, 1226419.
[28] D. Mukherjee, P. M. Austeris, S. Sampath, *ACS Energy Lett.* **2016**, *1*, 367-372.
[29] X. Wang, K. Du, Y. Y. Fredrik Liu, P. Hu, J. Zhang, Q. Zhang, M. H. S. Owen, X. Lu, C. K. Gan, P. Sengupta, C. Kloc, Q. Xiong, *2D Mater.* **2016**, *3*, 031009.
[30] F. Wang, T. A. Shifa, P. He, Z. Cheng, J. Chu, Y. Liu, Z. Wang, F. Wang, Y. Wen, L. Liang, J. He, *Nano Energy* **2017**, *40*, 673-680.
[31] T. A. Shifa, F. Wang, Z. Cheng, P. He, Y. Liu, C. Jiang, Z. Wang, J. He, *Adv. Funct. Mater.* **2018**, *28*, 1800548.
[32] Z. Cheng, T. A. Shifa, F. Wang, Y. Gao, P. He, K. Zhang, C. Jiang, Q. Liu, J. He, *Adv. Mater.* **2018**, *30*, 1707433.
[33] J. Zhang, R, Cui, X. Li, X. Liu, W. Huang, *J. Mater. Chem. A* **2017**, *5*, 23536-23542.
[34] J. Wang, Y. Zheng, F. Nie, J. Zhai, L. Jiang, *Langmuir* **2009**, *25*, 14129-14134.
[35] B. Song, K. Li, Y. Yin, T. Wu, L. Dang, M. Caban-Acevedo, J. Han, T. Gao, X. Wang, Z. Zhang, J. Schmidt, P. Xu, S. Jin, *ACS Catal.* **2017**, *7*, 8549-8557.
[36] W. Zhu, W. Gan, Z. Muhannad, C. Wang, C. Wu, H. Liu, D. Liu, K. Zhang, Q. He, H. Jiang, X. Zheng, Z. Sun, S. Chen, L. Song, *Chem. Commun.* **2018**, *54*, 4481-4484.
[37] G. Ouvrard, R. Brec, J. Rouxel, *Mater. Res. Bull.* **1985**, *20*, 1181-1189.
[38] M. Scagliotti, M. Jouanne, M. Balkanski, G. Ouvrard, G. Benedek, *Phys. Rev. B* **1987**, *35*, 7097.
[39] Y. Wang, D. Zhao, *Chem. Rev.* **2007**, *107*, 2821-2860.
[40] M. C. Biesinger, B. P. Payne, A. P. Grosvenor, L. W. M. Lau, A. R. Gerson, R. S. C. Smart, *Appl. Surf. Sci.* **2011**, *257*, 2717-2730.
[41] W. S. Xia, Y. Fan, Y. S. Jiang, Y. Chen, *Appl. Surf. Sci.* **1996**, *103*, I-9.
[42] F. Luo, H. Su, W. Song, Z. Wang, Z. Yan, C. Yan, *J. Mater. Chem.* **2004**, *14*, 111-115.
[43] C. C. Mayorga, Z. Sofer, D. Sedmidubsky, S. Huber, A. Y. S. Eng, M. Pumera, *ACS Appl. Mater. Interfaces* **2017**, *9*, 12563-12573.
[44] W. Li, Z. Wu, J. Wang, A. A. Elzatahry, D. Zhao, *Chem. Mater.* **2014**, *26*, 287-298.
[45] Y. C. Zhang, Z. N. Du, K. W. Li, M. Zhang, D. D. Dionysiou, *ACS Appl. Mater. Interfaces* **2011**, *3*, 1528-1537.
[46] Z. Cheng, F. Wang, T. A. Shifa, C. Jiang, Q. Liu, J. He, *Small* **2017**, *13*, 1702163.
[47] X. Lv, W. Wei, Q. Sun, F. Li, B. Huang, Y. Dai, *Appl. Catal. B-Environ.* **2017**, 217, 275-284.
[48] P.Zhao, Y. Ma, X. Lv, M. Li, B. Huang, Y. Dai, *Nano Energy* **2018**, 51, 533-538.
[49] J. Zhang, W. Zhu, X. Liu, *Dalton Trans.* **2014**, *43*, 9296-9302.
[50] M. Caban-Acevedo, M. L. Stone, J. R. Schmidt, J. G. Thomas, Q. Ding, H. Chang, M. Tsai, J. He, S. Jin, *Nat. Mater.* **2015**, *14*, 1245-1251.
[51] K. Yu, C. Zhang, Y. Chang, Y. Feng, Z. Yang, T. Yang, L. Lou, S. Liu, *Appl. Catal. B-Environ.* **2017**, *200*, 514-520.
[52] Y. Zhang, L. Wu, X. Zhao, Y. Zhao, H. Tan, X. Zhao, Y. Ma, Z. Zhao, S. Song, Y. Wang, Y. Li, *Adv. Energy Mater.* **2018**, *9*, 1801139.
[53] F. Wang, T. Shifa, P. Yu, P. He, Y. Liu, F. Wang, Z. Wang, X. Zhan, X. Lou, F. Xia, J. He, *Adv. Funct. Mater.* **2018**, *28*, 1802151
[54] T. Ohno, L. Bai, T. Hisatomi, K. Maeda, K. Domen, *J. Am. Chem. Soc.* **2012**, *134*, 8254-8259.
[55] W. Feng, L. Zhang, Y. Zhang, Y. Yang, Z. Fang, B. Wang, S. Zhang, P. Liu, *J. Mater. Chem. A* **2017**, *5*, 10311-10320.
[56] M. S. Faber, R. Dziedzic, M. A. Lukowski, N. S. Kaiser, Q. Ding, S. Jin, *J. Am. Chem. Soc.* **2014**, *136*, 10053-10061.
[57] X. Yang, A. Wolcott, G. Wang, A. Sobo, R. C. Fitzmorris, F. Qian, J. Z. Zhang, Y. Li, *Nano Lett.* **2009**, *9*, 2331-2336.
[58] J. Schneider and D. W. Bahnemann, *J. Phys. Chem. Lett.*, **2013**, *4*, 3479-3483.
[59] P. V. Kamat, and Jin, S. *ACS Energy Lett.*, **2018**, *3*, 622-623.
[60] X. Zhang, X. Zhang, J. Li, J. Sun, J. Bian, J. Wang, Y. Qu, R. Yan, C. Qin and L. Jing, *Appl. Catal. B-Environ.*, **2018**, *237*, 50-58.
[61] Q. Li, F. Zhao, C. Qu, Q. Shang, Z. Xu, L. Yu, J. R. McBride and T. Lian, *J. Am. Chem. Soc.*, **2018**, *140*, 11726-11734.
[62] Y. AlSalka, A. Hakki, J. Schneider and D. W. Bahnemann, *Appl. Catal. B-Environ.*, **2018**, *238*, 422-433.
[63] S. Fujita, H. Kawamori, D. Honda, H. Yoshida and M. Arai, *Appl. Catal. B-Environ.*, **2016**, *181*, 818-824.

10.1002/cssc.201900789

WILEY-VCH

FULL PAPER

Tailoring the porosity in iron phosphosulfide nanosheets to improve stability and efficiency of photocatalytic hydrogen evolution

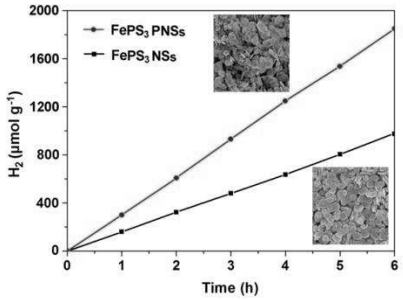

Jian Zhang, Fang Feng, Yong Pu, Xing'ao Li, Cher Hon Lau, and Wei Huang**

Tailoring the porosity in iron phosphosulfide nanosheets to improve performance of photocatalytic hydrogen evolution